NUCL SCI TECH (2017) 28:42
DOI 10.1007/s41365-017-0179-x

The study on the shrink-fit multi-ring flywheel with fall-off function

Yu-Jin Wang[1] · De-Zhong Wang[1] · Wei-Zhong Guo[1] · Jun-Lian Yin[1] · Cheng-Wei Wang[2]

Received: 18 September 2015 / Revised: 2 December 2016 / Accepted: 26 December 2016 / Published online: 17 February 2017

Abstract Structural integrity of the flywheel of reactor coolant pump is important for safe operation of a nuclear power plant. A shrink-fit multi-ring flywheel is designed with a fall-off function, i.e., it will separate from the shaft at a designed fall-off rotation speed, which is determined by the assembly process and the gravity. However, the two factors are ignored in the analytical method based on the Lame's equation. In this work, we conducted fall-off experiments to analyze the two factors and used the experimental data to verify the validity of the analytical method and the finite element method (FEM). The results show that FEM performs better than the analytical method in designing the fall-off function of the flywheel, though FEM cannot successfully predict the strain variation with the rotational speed.

Keywords Multi-ring flywheel · Fall-off rotational speed · Shrink-fit assembly · Gravity

1 Introduction

In a nuclear power plant (NPP), flywheels, with their kinetic energy storage, are used as uninterrupted power supply (UPS). If an accident happens, the flywheels keep running in a short time the reactor coolant pump to remove residual heat from the reactor core [1]. Flywheel can be seen as a hollow disk; its kinetic energy is $E = \pi h\rho(a^4 - b^4)\omega^2/8$ [2], where ρ is the density and h is the thickness. a and b *are* radii of the hollow disk, and ω is the angular velocity; a designer of a general-purpose flywheel can increase the density or the rotation speed [3]. In an NPP, the flywheels rotate at the same speed as a motor, so the high-density metal seems the only choice. Also, the structural integrity of the flywheel is important [1, 4, 5]. In this paper, we analyze a flywheel having a fall-off function to separate itself from the shaft sleeve at fall-off rotation speed, so as to avoid flywheel fracture.

The fall-off rotation speed is depended on the magnitude of shrink-fit, which is determined by the Lame's equation [6–10]. However, this equation works under the assumption of thick-wall cylinder in uniform thickness (ignoring the gravity effect), so the Lame's equation-based analytical method has been under questioning for its suitableness to solve complex structural engineering problems [11–14]. In addition, the fall-off function of flywheel is not studied systematically, but the shrink-fit failure without the gravity effect has been studied extensively. Antoni [15] studied the contact separation and failure of the two-ring disks with thermo-elastic–plastic analytical model and gave the critical rotational speed for plastic deform. Kovan [16] used the finite element method (FEM) to analyze the separation speed of interference-fit hollow shaft-hubs of different diameters and found that the separation speed was affected by the contact pressure resulted from the shrink-fit assembly. Sniezek et al. [17] investigated carrying capacity of the interference-fit assembly with a 3D finite element model and found that the calculated carrying capacity differed significantly from the experimental data, due to

This work was supported by the National Natural Science Foundation of China (No. 51576125).

✉ De-Zhong Wang
dzwang@sjtu.edu.cn

1 School of Mechanical Engineering, Shanghai Jiao Tong University, Shanghai 200240, China

2 Dalian Clean Energy Heavy Industrial Co., LTD, Dalian 116630, China

excessive mesh distortion in the simulation. By analysis of shrink-fit with FEM, Jiang et al. [18] suggested that the centrifugal force might be greater than the contact pressure at high speed, with decreased shrink-fit magnitude. Model simplification of different degrees is analyzed in the researches, but little has been done on experimental verification on the small radius-to-thickness ratio disks.

In this work, for studying those influence factors that have been ignored, flywheel fall-off experiments were conducted to record the rotation speed and strain variations, to verify validity of the analytical method and FEM by comparing the calculated results with the experimental data. Finite element models of different boundary conditions were built to evaluate the influence factors. The results show that the analytical method underestimates the fall-off rotation speed as it ignores the expansion sleeve connection, while the FEM results are close to the experiment data. Meanwhile, we measured the strain at some special position of the flywheel and found obvious gravity effect, but the FEM cannot successfully predict the variation tendency of the strain versus rotation speed.

Fig. 1 Configuration of the test platform

2 Experimental setup

An experimental setup was built to test the fall-off function of flywheel, as shown in Fig. 1. For safeguard against possible fracture of the fast-rotating flywheel, the flywheel itself is in an underground pit. The drive motor of the flywheel is 75 kW frequency-variable motor, and an inductor-type tachometer is used to measure the motor rotation speed.

The flywheel was assembled on the shaft in two processes. First, the flywheel was heated to a specific temperature so that the thermal dilation made its inner radius being larger than that of the shaft sleeve, and after natural cooling, the shrink-fit produced the residual stress. The second assembly process is expansion sleeve connection. By tightening the bolts (tension of about 1×10^6 N), the expansion sleeve deformed in the radial direction, and finally the shaft sleeve clinged to the shaft. The flywheel assembly is shown in Fig. 2a, and its specific parameters are listed in Table 1.

Three strain gages (KFG-03-120-C1-1121M2R, Kyowa) were pasted on the flywheel surface. As shown in Fig. 2b, gage A was pasted at the region where the flywheel contacted the shaft sleeve. If the fall-off process occurs, gage A will be fractured, with a sudden increase in the strain value. Gages B and C were pasted at $r = (a \cdot b)^{1/2}$, to measure the radial and tangential strain, respectively. The strain information was sent to a computer by the wireless

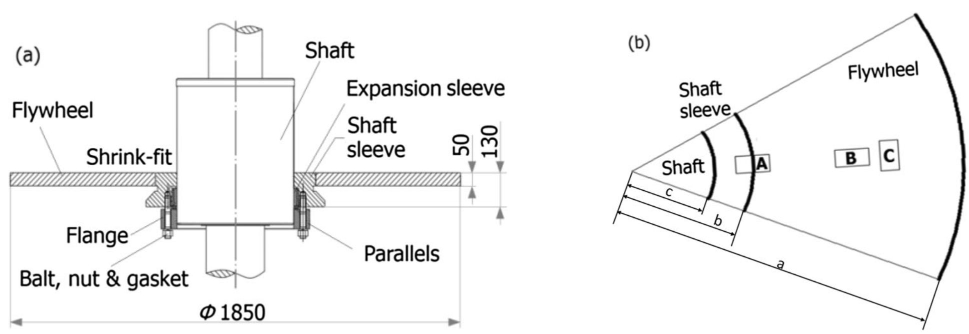

Fig. 2 Structure of the flywheel (**a**) and positions of the strain gages to test the fall-off function (**b**)

Table 1 Parameters of the flywheel

Material	Q235	Elastic modulus (E)	206 GPa
Flywheel outer radius (a)	925 mm	Density (ρ)	7850 kg/m^3
Flywheel inner radius (b)	330 mm	Poisson's ratio (μ)	0.3
Shaft inner radius (c)	270 mm	Shrink-fit (δ)	0.04 mm
Flywheel thickness (h)	50 mm	Rotation speed (Ω)	0–1800 rpm

strain node. Besides, the fall-off process of the flywheel was monitored by a high-speed camera.

3 Traditional design method

3.1 Magnitude of the shrink-fit

For designing a flywheel with the Lame's equation, the minimum and maximum allowable contact pressures ($cp_{\min}$ and $cp_{\max}$) can be calculated by Eqs. (1) and (2):

$$cp_{\min} = F/(Af) = \left[F_x^2 + (M_t/c)^2\right]^{1/2}/(2\pi ahf), \tag{1}$$

$$cp_{\max} = [\sigma]\left(b^2 - a^2\right)/\left(b^2 + a^2\right), \tag{2}$$

where F is the normal force on mating surface, A is the area of mating surface, f is the friction coefficients, F_x is the axial force related to the dead weight of flywheel, M_t is the maximum transmit moment of the motor, a, b and c are the radii, h is the height, and is the allowable stress of the material.

From the displacement magnitude of the mating surfaces, the shrink-fit δ can be calculated by [19]:

$$\delta = \frac{b \cdot cp}{E}\left(\frac{b^2 + c^2}{c^2 - b^2} + \mu\right) + \frac{b \cdot cp}{E}\left(\frac{a^2 + b^2}{b^2 - a^2} - \mu\right), \tag{3}$$

where E is elasticity modulus, and μ is the Poisson rate.

3.2 Fall-off rotational speed

To verify the fall-off function of flywheel, the radial stress on the mating surface is monitored. At 0 MPa of the radial stress, the contact status is open. Thus, the radial stress for rotating disks is the evaluation criteria of the fall-off function.

In analytical method, we assume that the disks are of uniform thickness and the thickness-to-diameter ratio is small enough to neglect the gravity [20]. Therefore, the general equilibrium equation can be written as

$$\frac{\mathrm{d}^2 u}{\mathrm{d}r^2} + \frac{1}{r}\frac{\mathrm{d}u}{\mathrm{d}r} - \frac{u}{r^2} + \left(1 - \mu^2\right)\frac{\rho\omega^2 r}{E} = 0, \tag{4}$$

where u is the displacement, $\omega = \Omega/60 \times 6.28$. Thus, we have:

$$u = -\left(1 - \mu^2\right)\frac{\rho\omega^2}{E}\frac{r^3}{8} + A_n r + \frac{B_n}{r}, \tag{5}$$

where A_n and B_n are the constants determined by the boundary conditions, and $n = 1$ or 2 is the serial number of the disks.

The radial strain (ε_r) and tangential strain (ε_r) are defined as

$$\varepsilon_r = \mathrm{d}u/\mathrm{d}r, \tag{6}$$

$$\varepsilon_t = u/r. \tag{7}$$

The radial stress (σ_r) and tangential stress (σ_t) of the rotating disks are given by [19]

$$\sigma_{rn}(r,\omega) = -\frac{3+\mu}{8}\rho\omega^2 r^2 + A_n - \frac{B_n}{r^2}, \tag{8}$$

$$\sigma_{tn}(r,\omega) = -\frac{3+\mu}{8}\rho\omega^2 r^2 + A_n + \frac{B_n}{r^2}. \tag{9}$$

For a two-disk model, A_1, A_2, B_1 and B_2 shall be determined under the four boundary conditions specified as follow

$$\sigma_{r1}(a,\omega) = 0, \tag{10}$$

$$\sigma_{r2}(c,\omega) = 0, \tag{11}$$

$$\sigma_{r1}(b,0) = \sigma_{r2}(b,0) = -cp, \tag{12}$$

$$\sigma_{r1}(b,\omega) = \sigma_{r2}(b,\omega). \tag{13}$$

Equations (10) and (11) express that there are no radial stress at free surface of the disks, and the radial stress has nothing to do with the rotation speed, so the radial stress is 0 MPa at any rotational speed. Equations (12) and (13) express that the two disks have the same radial stress on the mating surfaces based on the Newton's Third Law of Motion, and the magnitude of the radial stress equals to the contact pressure due to the shrink-fit when the flywheel is at rest.

Under these boundary conditions, and the A_1, A_2, B_1 and B_2 thus obtained, the radial stress and tangential stress of the two disks can be calculated as [20]

$$\sigma_{r1}(r,\omega) = \frac{3+\mu}{8}\rho\omega^2\left(a^2 - r^2\right) + \frac{a^2 b^2}{a^2 - b^2}cp\left(\frac{1}{a^2} - \frac{1}{r^2}\right), \tag{14}$$

$$\begin{aligned}\sigma_{t1}(r,\omega) = {} & -\frac{1+3\mu}{8}\rho\omega^2 r^2 + \frac{3+\mu}{8}\rho\omega^2 a^2 \\ & + \frac{a^2 b^2}{a^2 - b^2}cp\left(\frac{1}{a^2} + \frac{1}{r^2}\right),\end{aligned} \tag{15}$$

$$\begin{aligned}\sigma_{r2}(r,\omega) = {} & \frac{3+\mu}{8}\rho\omega^2\left(c^2 - r^2\right) + \frac{b^2 c^2}{b^2 - c^2} \\ & \times\left[-cp + \frac{3+\mu}{8}\rho\omega^2\left(a^2 - c^2\right)\right]\left(\frac{1}{c^2} - \frac{1}{r^2}\right),\end{aligned} \tag{16}$$

$$\begin{aligned}\sigma_{t2}(r,\omega) = {} & -\frac{1+3\mu}{8}\rho\omega^2 r^2 + \frac{3+\mu}{8}\rho\omega^2 c^2 \\ & + \frac{b^2 c^2}{b^2 - c^2}\left[-cp + \frac{3+\mu}{8}\rho\omega^2\left(a^2 - c^2\right)\right] \\ & \times\left(\frac{1}{c^2} + \frac{1}{r^2}\right).\end{aligned} \tag{17}$$

4 Finite element models

For comparing the analytical results with experimental data, 2-D axisymmetric FE models of the flywheel assembly are established with ANSYS 14.5. The flywheel is modeled with the axisymmetric PLANE42 elements, and the contact pairs are modeled with CONTA172 and TARGE169 elements. In this paper, five FE models are simplified to different degrees in their assembly models and boundary conditions, as shown in Table 2.

As shown in Fig. 3, Model 0 is a shrink-fit two-ring two-disk flywheel of uniform thickness; Model 1 is a flywheel of the shaft sleeve type, without the expansion sleeve connection, while Models 2, 3 and 4 are of the same geometry but different boundary conditions. Model 2 is a flywheel of stationary state, considering no effect of the gravity. Model 3 rotates, but no gravity effect for Model 3. Model 4, being the most complex of all models, rotates with the gravity effect.

To analyze sensitivity of the grid, the Model 0 has two grid settings (the numbers in Fig, 4a denote the elements along the edges). By comparing the stress distribution along a node path (the red arrows), a proper density of grid is determined.

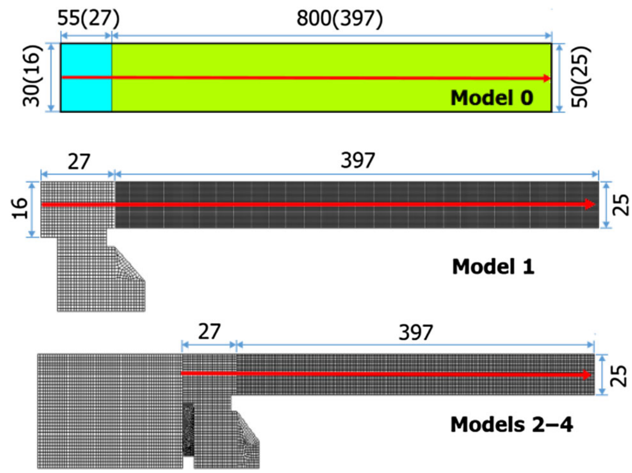

Fig. 3 FE flywheel assembly model

5 Results and discussion

5.1 Mesh-sensitiveness

The study is conducted with Model 0 of two element densities (800 × 50 in the radial direction and 397 × 25 in axial direction), and the stress distributions are compared with those calculated by the Lame's equation. Stress distributions along the radial direction by Lame and FEM are shown in Fig. 4. It can be seen that the two models are of sufficient accuracy for the present study. And for shrink-fit disks with uniform thickness, the two methods have almost the same results. The curve of Model 1 is also plotted in Fig. 5; the difference is not obvious among the three curves.

5.2 Influence factors

5.2.1 Expansion sleeve connection process

In assembling the expansion sleeve, when the bolts are tightened, the contact pressure produced by expanding the sleeve causes radial deformation of the shaft, and the stress distribution is influenced due to magnitude increase in the shrink-fit. The radial and tangential stress distributions are shown in Fig. 5. Obviously, the radial stress (contact pressure) on mating surface is greater than the analytical method, and the tangential stress distributions show that tangential tensile deform occurred to the flywheel and shaft sleeve.

5.2.2 Gravity effect

The shrink-fit multi-ring flywheel has a special geometry feature: a small thickness-to-radius ratio ($\approx$0.054). Therefore, under the action of gravity, the flywheel bends naturally, just like a cantilever beam. Originally, the gravity is ignored based on the Lame assumption of the thick-wall cylinder. The gravity effect is studied by comparing the stress distribution by FEM of Models 3 and 4.

Table 2 FEM models for flywheel

No.	Parts				Boundary condition		
	Flywheel	Shaft sleeve	Expansion sleeve	Shaft	Tightened Bolts	Gravity	Rotational speed
0	Y	Y[a]	N	N	N	N	N
1	Y	Y	N	N	N	N	N
2	Y	Y	Y	Y	Y	N	N
3	Y	Y	Y	Y	Y	N	Y
4	Y	Y	Y	Y	Y	Y	Y[b]

[a] Shaft is modeled based on the Lame assumptions

[b] Rotational speed are 300, 600, 900 and 975 rpm

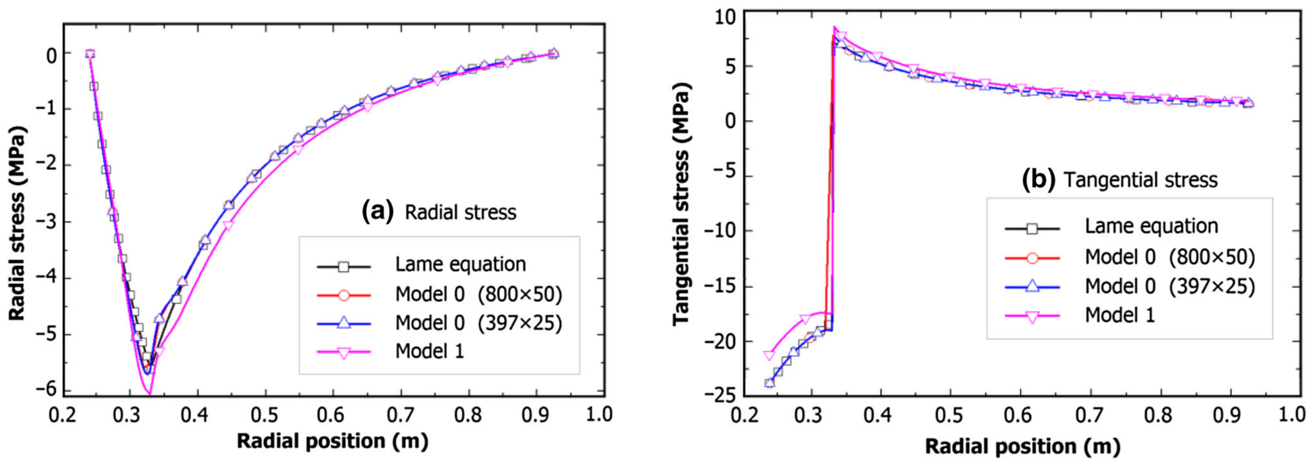

Fig. 4 Stress distributions obtained by the Lame equation and FEM (Models 0 and 1)

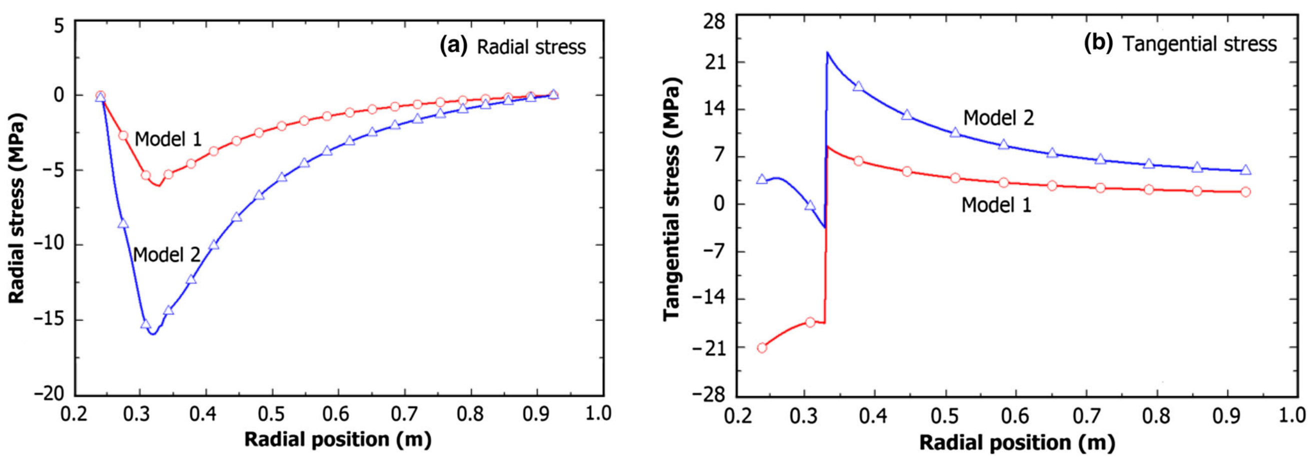

Fig. 5 Influence of the expansion sleeve on stress distribution of the shrink-fitted flywheel

The stress distributions under different rotation speeds are shown in Fig. 6, in which 'w/o' means the FE results without considering gravity; otherwise, the data are labeled as 'w/'. It is hard to find that there is no difference at any rotational speed. However, the experimental results are not consistent with the FEA results.

5.3 Fall-off rotation speed

The contact pressure (radial stress) at inner edge of the flywheel is monitored to judge the contact status (Fig. 7). The contact pressure decreases with increasing rotation speed, and the contact status is open at 465 rpm,

The simulations of fall-off process of the flywheel are performed with Models 1 and 4, ignoring the roughness of the mating surface. A fall-off happens when the flywheel is running to the critical rotation speed and the contact pressure is zero. Figure 8 shows the contact pressure distribution along the mating surface at different rotation speeds. The two predictions of the fall-off rotation speed are different, being about 665 rpm for Model 1, and about 975 rpm for Model 4. So, the tightened expansion sleeve has an increased magnitude of shrink-fit, so the expansion sleeve connection should not be ignored.

5.4 Experimental results

Readings of the strain gage A are shown in Fig. 9, with a sudden increase at the fall-off rotation speed, due to failure of the strain gage. Figure 9b shows the fall-off process shot by high-speed camera. The flywheel dropped on the conical surface of the shaft sleeve, at rotation speed of 1120 and 1040 rpm in two experiments, respectively. The different speeds are related to the uncontrolled pretension force of the bolts in the expansion sleeve assembly process, which affects the shrink-fit magnitude of the flywheel.

The predicted fall-off rotation speeds are 465 rpm by the analytical method, and 665 and 975 rpm by FEM for Models 1 and 4, respectively, while the measured data are 1040 and 1120 rpm. While the analytical method provides

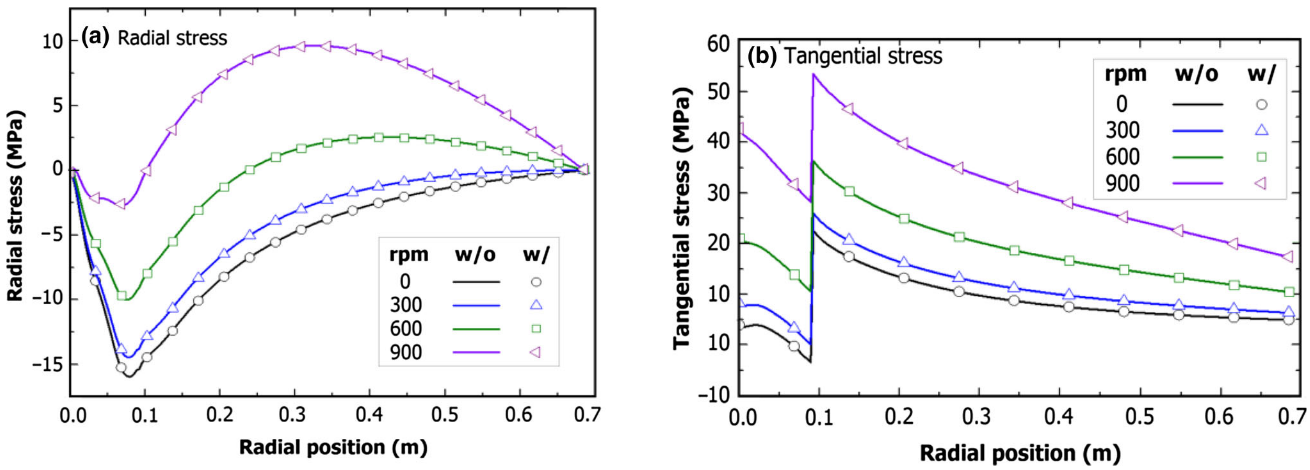

Fig. 6 Influence of gravity on the stress distribution at different rotational speeds

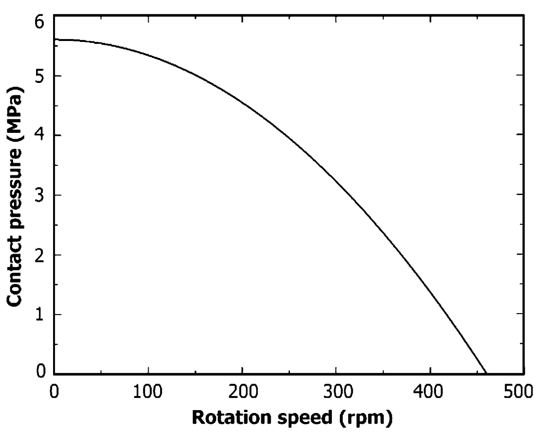

Fig. 7 Contact pressure versus rotation speed

a false fall-off rotation speed, the result of FEM (Model 4) considering the expansion sleeve connection is close to the measured data.

In the experiment, we analyzed the force balance between the gravity and centrifugal force by observing the radial and tangential strains. Strain gages B and C were pasted at locations introduced in Fig. 2a. The results are plotted in black squares in Fig. 10. At low rotation speeds, the centrifugal force is less than the gravity, so the flywheel deforms like a bend cantilever, while at high rotation speeds, the flywheel will be lifted to parallel to the horizon by the centrifugal force. The radial strain gage was under compression during the flywheel-lifting process. When the centrifugal force increases, the radial elongation of flywheel becomes obvious gradually, so the strains change from negative to positive, as plotted in Fig. 10.

Figure 10 also shows the simulation results of force balance analysis using Model 4. In this simulation, gravity was the only load considered in Step 1, and the rotation was added in Step 2. The radial strain ε_r for FEM analysis was obtained by

$$\varepsilon_r = (l_2 - l_1)/l_1, \tag{18}$$

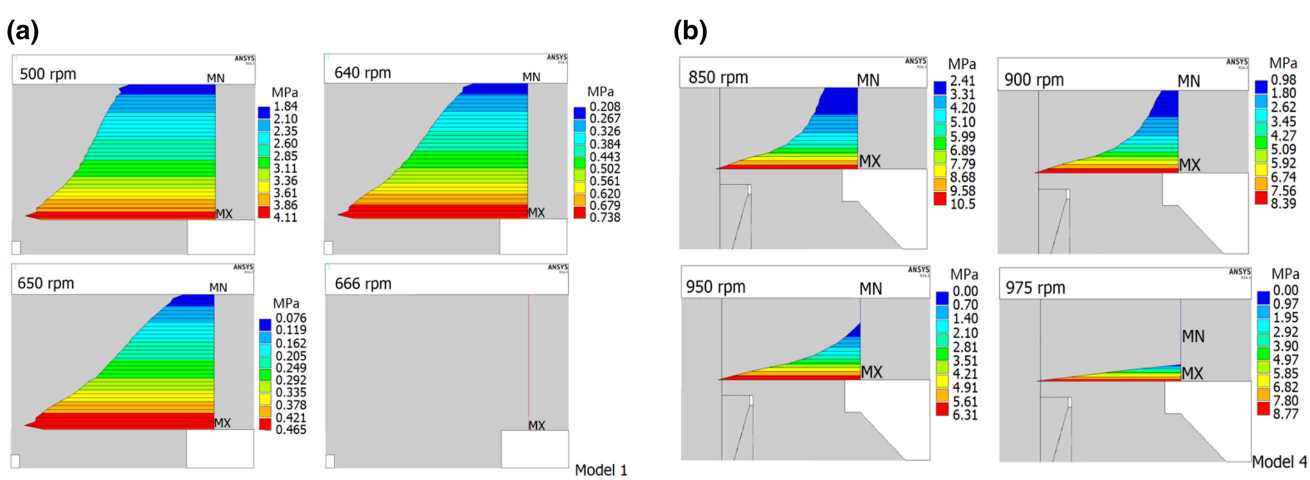

Fig. 8 Contact pressures of Model 1 (**a**) and Model 4 (**b**)

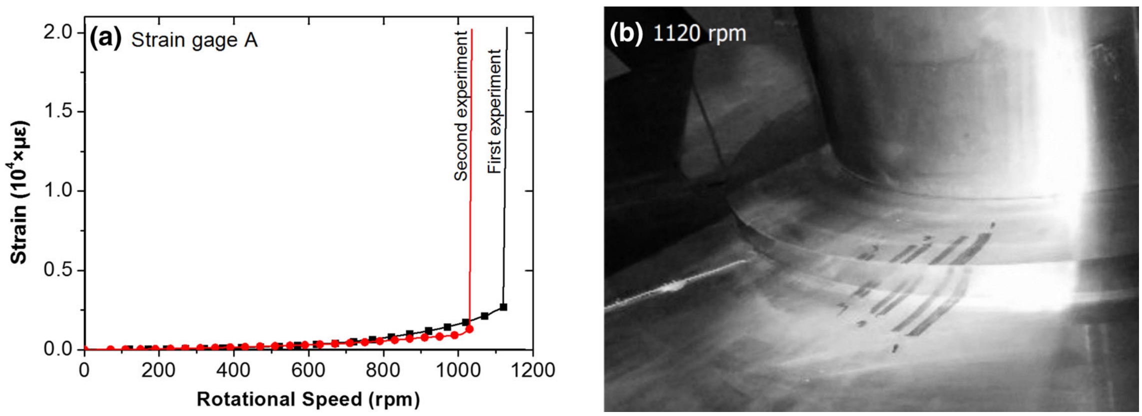

Fig. 9 Readings of the strain gage A versus rotation speed (**a**) and the fall-off process (**b**) of the flywheel

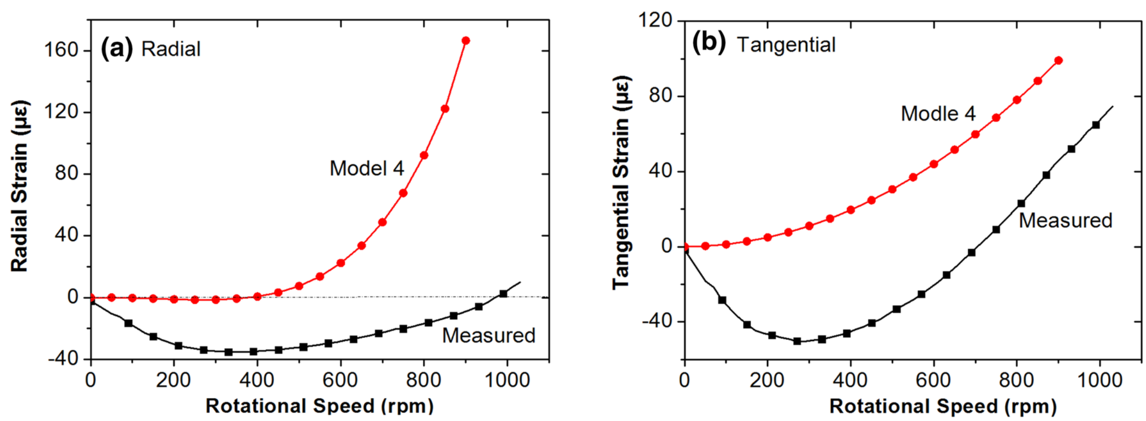

Fig. 10 Comparison of the measured and FEM-predicted strains of the flywheel

where l is the edge length of the monitored element, and the subscripts denote different load steps in this analysis. The strain varying with the rotation speed is plotted in red full circles in Fig. 10. Although the FEM-predicted fall-off rotation speed is close to the experimental data, the calculated strains are not consistent with the measurement. Although it is unclear what causes the significant difference, the experimental results show the necessity of taking the gravity effect into account.

In addition, other interesting phenomena are valuable to further study. The experimental results show the tangential strain has the same variation tendency as radial strain, and the minimum tangential strain is lower than the radial strain at low rotation speed, indicating that the tangential compression deform is more obvious than radial strain.

6 Conclusion

The fall-off function of shrink-fit multi-ring flywheel of RCP has been studied. The fall-off rotation speed and changes in strain measured in experiments are used to verify the validity of the analytical method and FEM. The influence factors ignored in the analytical method are analyzed. The following conclusions can be made:

1. The analytical method is not suitable to predict the fall-off rotation speed of shrink-fit flywheel of complex structure.
2. The influence of expansion sleeve connection should be considered in engineering design. FEM-predicted fall-off rotation speed is close to the measured speed.
3. The FEM-predicted strains deviate from the experimental results, so FEM underestimates the gravity effect, and the mechanism behind this phenomenon requires further investigations.

Overall, FEM is a better choice to replace the analytical method from an engineering view.

References

1. NRC U S. Nureg 1.14. (1975)
2. B. Bolund, H. Bernhoff, M. Leijon, Flywheel energy and power storage systems. Renew. Sustain. Energy Rev. **11**, 235–258 (2007). doi:10.1016/j.rser.2005.01.004

3. G. Genta, *Kinetic Energy Storage* (Butterworths, London, 1985)
4. NRC U S. Nureg 0800. (1987)
5. J.S. Park, H.C. Song, K.S. Yoon et al., Structural integrity evaluation for interference-fit flywheels in reactor coolant pumps of nuclear power plants. J. Mech. Sci. Technol. **19**, 1988–1997 (2005). doi:10.1007/BF02916491
6. Westinghouse Electric Corporation Structural analysis summary for the ap1000 reactor coolant pump high inertia flywheel. (2006)
7. Mitsubish Heavy Industries L, Structural analysis for us-apwr reactor coolant pump motor flywheel. (2007)
8. J.M. Wang, J.F. Kang, L. Tang, Theoretical and experimental studies for wind turbine's shrink disk. Proc. Inst. Mech. Eng. C J. Mech. **229**(2), 325–334 (2015). doi:10.1177/0954406214533529
9. C.E. Truman, J.D. Booker, Analysis of a shrink-fit failure on a gear hub/shaft assembly. Eng. Fail. Anal. **14**, 557–572 (2007). doi:10.1016/j.engfailanal.2006.03.008
10. S. Bhowmick, D. Misra, K.N. Saha, Parametric study of externally loaded rotating discs under shrink fit. Proc. Inst. Mech. Eng. C J. Mech. **224**, 2525–2538 (2010). doi:10.1243/09544062jmes1996
11. Y. Zhang, B. McClain, X.D. Fang, Design of interference fits via finite element method. Int. J. Mech. Sci. **42**, 1835–1850 (2000). doi:10.1016/S0020-7403(99)00072-7
12. A. Özel, S. Temiz, M.D. Aydin et al., Stress analysis of shrink-fitted joints for various fit forms via finite element method. Mater. Des. **26**, 281–289 (2005). doi:10.1016/j.matdes.2004.06.014
13. M.A. Kutuk, O. Eyercioglu, N. Yildirim et al., Finite element analysis of a cylindrical approach for shrink-fit precision gear forging dies. Proc. Inst. Mech. Eng. C J. Mech. **217**, 677–685 (2003). doi:10.1243/095440603321919590
14. O. Eyercioglu, M.A. Kutuk, N.F. Yilmaz, Shrink fit design for precision gear forging dies. J. Mater. Process. Technol. **209**, 2186–2194 (2009). doi:10.1016/j.jmatprotec.2008.05.016
15. N. Antoni, Contact separation and failure analysis of a rotating thermo-elastoplastic shrink-fit assembly. Appl. Math. Model. **37**, 2352–2363 (2013). doi:10.1016/j.apm.2012.05.018
16. V. Kovan, Separation frequency analysis of interference fitted hollow shaft–hub connections by finite element method. Adv. Eng. Softw. **42**, 644–648 (2011). doi:10.1016/j.advengsoft.2011.05.001
17. L. Sniezek, J. Zimmerman, A. Zimmerman, The carrying capacity of conical interference-fit joints with laser reinforcement zones. J. Mater. Process. Technol. **210**, 914–925 (2010). doi:10.1016/j.jmatprotec.2010.02.004
18. F.L. Jiang, Z.Q. Liu, G. Liu, Modeling and fem analysis for interference between tool shank and shrink fit toolholder. Adv. Mater. Res. **328–330**, 446–450 (2011). doi:10.4028/www.scientific.net/AMR.328-330.446
19. S. Timoshenko, *Strength of Materials Part II Advanced Theory and Problems* (Van Nostrand Reinhold Company, London, 1958)
20. S.M.M. Jafri, Analysis of shrink fit interface stresses for rotating circular disks. ASME Turbo Expo **5**, 275–283 (2007). doi:10.1115/GT2007-27109